BRAIN IMAGING

Whole-brain spatial transcriptional analysis at cellular resolution

Shigeaki Kanatani[1]*, Judith C. Kreutzmann[1]†, Yue Li[1]†, Zoe West[1]†, Lea Lydolph Larsen[2], Danai Vougesi Nikou[1], Ilse Eidhof[1], Abigail Walton[1], Songbai Zhang[1], Leslie Rubio Rodríguez-Kirby[1], Jacob Lercke Skytte[2], Casper Gravesen Salinas[2], Kimiharu Takamatsu[1,3], Xiaofei Li[4], Daisuke H. Tanaka[5,6], Dagmara Kaczynska[1], Keishiro Fukumoto[1,3], Razieh Karamzadeh[1], Yujiao Xiang[7], Naofumi Uesaka[6], Tsutomu Tanabe[5], Mikael Adner[7], Johan Hartman[8,9], Ayako Miyakawa[1,10], Erik Sundström[4], Gonçalo Castelo-Branco[1], Urmas Roostalu[2], Jacob Hecksher-Sørensen[2], Per Uhlén[1]*

Recent advances in RNA analysis have deepened our understanding of cellular states in biological tissues. However, a substantial gap remains in integrating RNA expression data with spatial context across organs, primarily owing to the challenges associated with RNA detection within intact tissue volumes. Here, we developed Tris buffer–mediated retention of in situ hybridization chain reaction signal in cleared organs (TRISCO), an effective tissue-clearing method designed for whole-brain spatial three-dimensional (3D) RNA imaging. TRISCO resolved several crucial issues, including the preservation of RNA integrity, achieving uniform RNA labeling, and enhancing tissue transparency. We tested TRISCO using a broad range of cell-identity markers, noncoding and activity-dependent RNAs, within diverse organs of varying sizes and species. TRISCO thus emerges as a powerful tool for single-cell, whole-brain, 3D imaging that enables comprehensive transcriptional spatial analysis across the entire brain.

Three-dimensional (3D) visualization of molecules on the whole-brain scale is essential to understand the spatial relationships of cells and the circuits in which they participate (*1*, *2*). Multiple tissue-clearing protocols for imaging volumes have been published, the vast majority of which focus on assessments of the distribution of proteins rather than RNA transcripts (*3*, *4*). Although a few pioneering protocols have attempted to combine RNA imaging with tissue clearing (*3*, *5*), application to larger tissues, such as entire mammalian brains, remains challenging.

In situ hybridization, a common technique for detecting RNA in fixed cells, traditionally uses digoxigenin-labeled RNA probes and enzyme-based signal amplification by alkaline phosphatase or horseradish peroxidase (*6*). However, enzyme-based signal amplification has been reported to generate a disproportionate brain signal gradient that is higher near the surface of the brain than at the center, rendering it highly ineffective for 3D imaging (*3*). Hybridization chain reaction (HCR) is an enzyme-free amplification method, whereby metastable hairpin oligonucleotides are triggered to undergo a chain reaction upon binding of an "initiator" sequence (*7*). This signal amplification technique has undergone several enhancements over the years, resulting in a third generation of improvements. It has been successfully applied to various research applications, including developmental biology, neuroscience, and cancer research (*8*, *9*). We recently developed the diagnosing in situ immunofluorescence-labeled cleared oncosamples (DIIFCO) technique, which combines in situ HCR (isHCR) with organic solvent clearing (*5*), to study RNAs in mouse embryos, brain sections, and clinical biopsies. Given the high demand for whole-brain spatial transcriptional analysis (*2*), we assessed DIIFCO on adult whole-brain samples but concluded that this method was unsuitable for visualizing RNA across intact brains owing to issues with poor RNA integrity, inhomogeneous labeling, and weak transparency.

In this work, we present a new technique, Tris buffer–mediated retention of isHCR signal in cleared organs (TRISCO), which can perform spatial RNA analysis of whole brains with homogeneous isHCR signal and high tissue transparency after organic solvent clearing (*10*, *11*). We demonstrate that TRISCO offers a straightforward methodology for achieving whole-brain 3D imaging at single-cell resolution, capturing a comprehensive array of transcripts, thereby uncovering the transcripti landscapes across the entire brain.

[1]Division of Molecular Neurobiology, Department of Medical Biochemistry and Biophysics, Karolinska Institutet, Stockholm, Sweden. [2]Gubra ApS, Hørsholm, Denmark. [3]Department of Urology, Keio University School of Medicine, Tokyo, Japan. [4]Division of Neurogeriatrics, Department of Neurobiology, Care Sciences and Society, Karolinska Institutet, Stockholm, Sweden. [5]Department of Pharmacology and Neurobiology, Graduate School of Medical and Dental Sciences, Tokyo Medical and Dental University (TMDU), Tokyo, Japan. [6]Department of Cognitive Neurobiology, Graduate School of Medical and Dental Sciences, Institute of Science Tokyo, Tokyo, Japan. [7]Institute of Environmental Medicine, Karolinska Institutet, Stockholm, Sweden. [8]Department of Oncology-Pathology, Karolinska Institutet, Stockholm, Sweden. [9]Department of Clinical Pathology and Cancer Diagnostics, Karolinska University Hospital, Stockholm, Sweden. [10]Division of Urology, Department of Molecular Medicine and Surgery, Karolinska University Hospital, Stockholm, Sweden.
***Corresponding author. Email: shigeaki.kanatani@ki.se (S.K.); per.uhlen@ki.se (P.U.)**
†These authors contributed equally to this work.

Combining isHCR with organic solvent tissue clearing

Existing protocols for RNA imaging in tissues are restricted to ultrathin sections or samples only a few millimeters thick because of methodological challenges, such as uneven probe penetration, compromised RNA integrity, low signal intensity, and reduced tissue transparency following clearing procedures. To enable whole-brain imaging, we sought to overcome these obstacles. Firstly, we aimed to mitigate the impact of ribonuclease (RNase) contamination and RNA degradation during in situ hybridization experiments. For this, we adapted the DIIFCO pipeline (*5*), modifying the process by eliminating all steps where RNase can be active prior to hybridization: low-percentage methanol treatment, washing with aqueous buffers, and blocking with donkey serum (fig. S1, A and B). To protect RNA integrity, we directly transferred the samples from 100% methanol to 50% formamide, which has been shown to inhibit RNase activity (*12*). Additionally, we used polyvinylsulfonic acid (PVSA), a cost-effective RNase inhibitor with a half-maximal inhibitory concentration of 0.15 mg/mL against RNase A (*13*). To confirm that PVSA did not affect isHCR RNA labeling, we visualized paravalbumin (*Pvalb*) mRNA in mouse cerebellum sections and assessed signal intensity (Fig. 1A). PVSA had no effect on the *Pvalb* isHCR signal intensity (Fig. 1B), even at high concentrations (fig. S1, C and D); therefore, we proceeded with using PVSA in our pipeline.

With DIIFCO, we occasionally observed suboptimal tissue transparency for imaging RNA in the entire adult brain. To address this issue, we tested possible causes of insufficient clearing. We found that treating brains with 5× saline-sodium citrate (SSC) buffer and Tween20 (5×SSCT), a well-established and essential step in the standard isHCR protocol, markedly reduced the effectiveness of tissue clearing (Fig. 1C). By contrast, washing the brains with water prior to the clearing process substantially improved tissue transparency. We quantified sample transparency by analyzing the intensity profile along a line through the cross section of a brain labeled with green nuclear staining dye DiYO-1 (Fig. 1D) and by assessing the visibility of the grid beneath the brain (Fig. 1E). These analyses showed poor transparency in the center of brains incubated in 5×SSCT. In addition, when assessing the signal intensity ratio between a region inside the brain and a region outside the brain, we found significantly reduced transparency in brains treated with 5×SSCT compared with those washed with water (Fig. 1F) [one-way analysis of variance (ANOVA), $F_{2,16} = 37.80$, $P < 0.0001$].

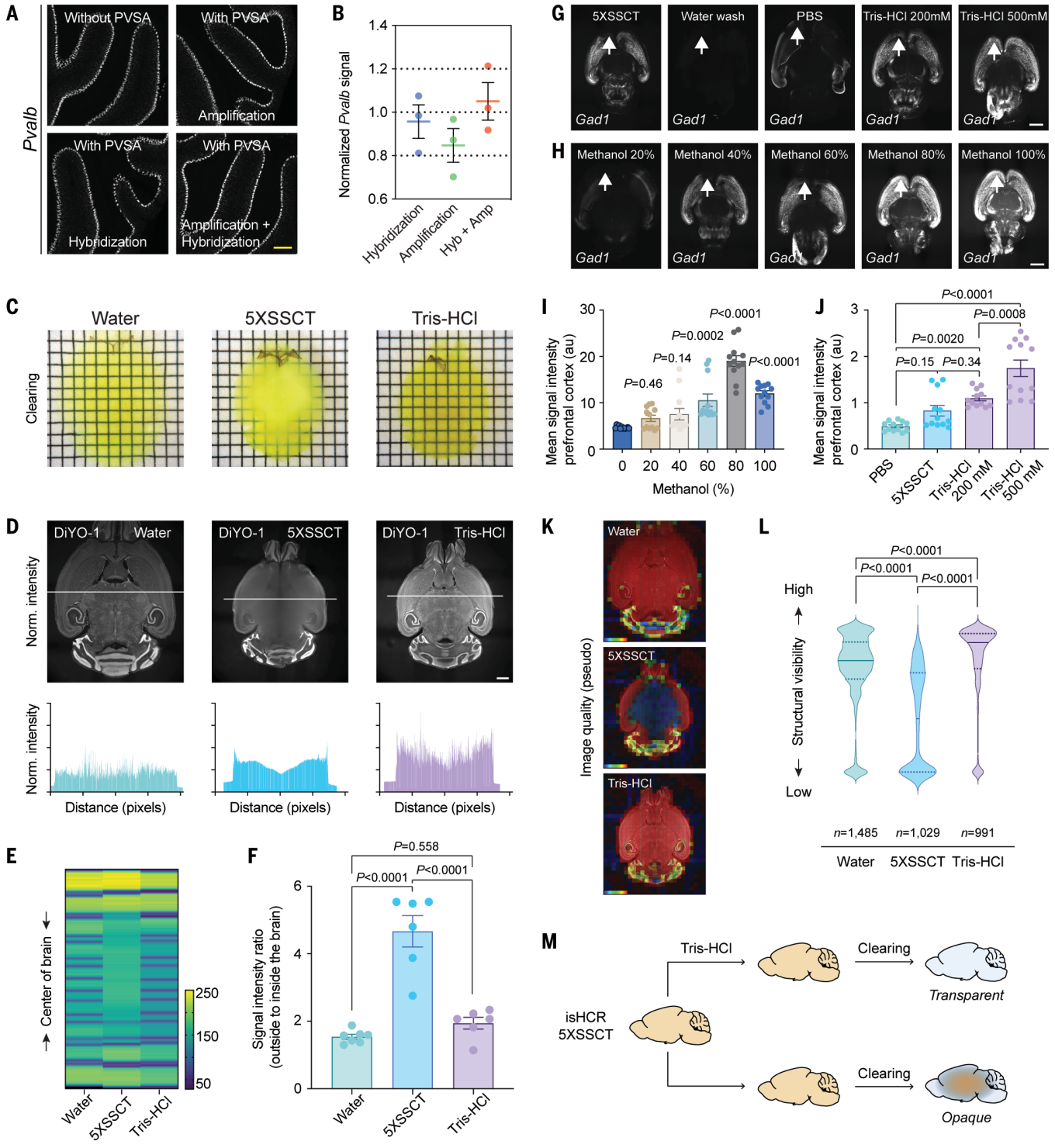

Fig. 1. Merging isHCR and iDISCO. (**A** and **B**) Tissue sections of cerebellum stained by using isHCR for *Pvalb* mRNA treated with the RNase inhibitor polyvinyl sulfonic acid (PVSA) (3.8 mg/mL) introduced in either the amplification (Amp) buffer, hybridization (Hyb) buffer, or both (Hyb + Amp) (A) as well as quantitative analysis of signal intensities normalized to measurements obtained without PVSA (B). (**C** and **D**) Whole brains cleared by using iDISCO prewashed with water, 5×SSCT, or Tris-HCl and imaged on gridded paper (C) (grid lines, 1 mm) and optical cross sections of brains nuclear stained with DiYO-1 and intensity profiles (below) measured at indicated lines (D). (**E**) Graph illustrating the visibility of grid lines through brains cleared using the specified treatments. (**F**) Quantitative analysis of the signal intensity ratio between a region inside and outside the brain (n = 6 to 7 ROIs from 3 brains, one-way ANOVA, $F_{2,16}$ = 37.80, P < 0.0001). (**G** to **J**) Optical cross sections of whole brains from newborn (P0-1) mice stained by using isHCR for *Gad1* mRNA, subjected to a 4-day wash with either 5×SSCT, water, PBS, 200-mM Tris-HCl, or 500-mM Tris-HCl (G) or 20, 40, 60, 80, or 100% methanol (H) and quantitative analysis of the signal intensities in the prefrontal cortex [(I) one-way ANOVA, $F_{5,66}$ = 28.74, P < 0.0001; (J) one-way ANOVA, $F_{3,44}$ = 23.06, P < 0.0001]. The signal intensity was normalized to the mean intensity in the thalamus. (**K**) Pseudo-colored image quality analysis of optical cross sections depicted in (D). Red signifies

high-quality regions, whereas blue signifies low-quality regions. (**L**), Violin plot of the structural visibility using water, 5×SSCT, or Tris-HCl (one-way ANOVA, $F_{2,3502}$ = 566.2, P < 0.0001). (**M**) Schematic of merging of isHCR with iDISCO clearing, with or without Tris-HCl washing. Scale bars, 1 mm (white) and 200 μm (yellow). All data are shown as the mean ± SEM. Statistical analysis was performed using one-way ANOVA with Tukey's [(F) and (L)] or Dunnett's [(I) and (J)] post hoc comparison.

Our next focus was to maintain the fluorescence pattern of the isHCR labeling following tissue clearing. We stained newborn mouse brains with in house–designed DNA oligonucleotide probes targeting Glutamate decarboxylase 1 (*Gad1*) mRNA using a set of 35 probes and thereafter performed tissue clearing. The *Gad1* isHCR staining was primarily observed at the surface of the brain, including areas such as the cerebral cortex and striatum, whereas deeper areas such as the thalamus showed little to no staining (Fig. 1G). When the brains were washed with water, which was favorable for tissue clearing (Fig. 1C), the *Gad1* isHCR signal was completely lost (Fig. 1G). Given that stable hybridization requires salt, we tested washing the brains with phosphate-buffered saline (PBS). Although PBS preserved the isHCR signal to some extent, it was insufficient for maintaining a robust signal. After testing several buffers, we found that Tris effectively retained the isHCR *Gad1* signal (Fig. 1G) while also ensuring efficient tissue clearing (Fig. 1C), likely because Tris dissolves in high concentrations of methanol without forming precipitates. However, at a lower concentration of 200 mM, faint staining remained in restricted regions, likely due to weak hybridization stability caused by a low amount of salt. To test this hypothesis, we increased the Tris-HCl buffer concentration to 500 mM. At this higher concentration, the previously dark regions were eliminated, resulting in a more homogeneous staining throughout the tissue. Compared with the 5×SSCT buffer, 500-mM Tris-HCl markedly improved the tissue clearing (Fig. 1, D and E) and significantly enhanced transparency (Fig. 1F) (one-way ANOVA, $F_{2,16}$ = 37.80, P < 0.0001). We then assessed how isHCR labeling was affected by dehydration, a crucial step in organic solvent-based tissue clearing (*5*, *14*). In comparing signal intensities in the prefrontal cortex, we found that initiating the wash with >80% methanol yielded strong and uniform signal intensity (Fig. 1, H and I). Based on these results, we proceeded with using >80% methanol.

To assess the optical transparency, contrast, and level of detail in the images generated by our method, we used a machine learning model pretrained on high-quality images (materials and methods). This analysis revealed that 500-mM Tris-HCl produced better overall image quality compared with 5×SSCT, particularly in the central regions of the brain (Fig. 1, K and L). We subsequently used 500-mM Tris-HCl to wash out the SSC, ensuring hybridization stability and preventing precipitation during the organic solvent clearing process (Fig. 1M).

Tissue penetration and uniform staining

We and others have successfully performed isHCR in tissue volumes of limited size (*3*, *5*). However, when scaling up to whole-brain samples, we observed inconsistent results, characterized by intense surface staining but little to no signal in deeper regions (Fig. 2A, left). To address this issue, we first explored whether applying higher amounts of DNA hairpins would provide a uniform staining. Three different volumes of hairpin DNA, 24, 48, and 96 pmol, were tested on whole brains stained for *Gad1* mRNA. The two- and fourfold increase in hairpin DNA amount resulted in a marginal improvement in penetration (fig. S2B), but it was not sufficient to label *Gad1*-positive regions across the whole brain volume, which were detectable in tissue sections using conventional isHCR (fig. S2C). We then labeled a target with a homogeneous expression, *Thy1* mRNA, and increased volume and hairpin amount eightfold (192 pmol); however, this also failed to yield adequate signal intensity in the deeper regions (fig. S2, D and E).

To investigate the penetration issue in more detail, we evaluated several strategies that could affect the isHCR process, including modifications to buffer composition, adjustments to incubation times, the application of pressure, and the use of centrifugation and electrophoresis. However, none of these approaches led to a marked improvement. We then shifted our focus to examining the impact of temperature on whole-brain isHCR staining. We designed DNA probes targeting *Thy1* mRNA consisting of 27 probes and performed whole-brain staining using isHCR. At 37° and 20°C, the surface isHCR signal intensity for *Thy1* was saturated, whereas staining in deeper regions was weak (Fig. 2, B and C). By contrast, at 4°C, we observed a substantial reduction in surface signal intensity with improved staining in deeper regions. This result prompted us to further assess the impact of temperature on isHCR signal intensity. We sectioned mouse cerebellums and stained *Pvalb* mRNA at temperatures ranging from 70° to 4°C (Fig. 2D). These experiments showed that room temperature (20°C) yielded the strongest isHCR signals, consistent with standard protocols. However, we observed that *Pvalb* mRNA signals remained detectable even at 4°C, albeit at a lower intensity than at room temperature, demonstrating that HCR could still occur at this low temperature (fig. S3).

To further explore the effect of temperature on tissue penetration, we designed a probe targeting homogenously expressed *Malat1* mRNA consisting of 127 probes. At 37° and 20°C, almost only the surface was stained, as deeper regions were dark (Fig. 2, E and F). At 4°C, we observed a reduction in surface signal intensity with improved signal intensity in deeper regions (Fig. 2D). Quantitative analysis revealed significantly enhanced structural visibility across the whole brain at 4°C for both *Thy1* mRNA (Fig. 2, G and H) (one-way ANOVA, $F_{2,2102}$ = 63.59, P < 0.0001) and *Malat1* mRNA (Fig. 2, I and J) (one-way ANOVA, $F_{2,3115}$ = 530.9, P < 0.0001). These experiments indicated that lower temperatures facilitated more homogeneous staining across large tissue volumes. The reduction in surface signal was likely due to the slower kinetics of the HCR at lower temperatures, allowing a greater number of hairpins to penetrate deeper into the tissue before undergoing HCR signal amplification and preventing them from being depleted at the surface (Fig. 2A, right).

TRISCO enables whole-brain RNA imaging at single-cell resolution

After establishing all steps of the protocol, we performed 3D imaging of whole mouse brains using the complete TRISCO pipeline: paraformaldehyde fixation, delipidation, bleaching, blocking, hybridization, washing, temperature-controlled hairpin probe incubation, Tris-HCl washes, and organic solvent clearing (Fig. 3A). Additionally, we found that DiYO-1 could be introduced during the DNA hybridization phase. In a whole brain from an 8-week-old mouse, we readily detected RNAs of *Pvalb*, *Gad1*, and *Somatostatin* (*Sst*) in combination with nuclear staining with DiYO-1 (Fig. 3B and movies S1 and S2). Landmarks of the brain, such as the neocortex and hippocampus, were clearly discernible. TRISCO's cellular resolution revealed overlapping and distinct expression patterns of *Pvalb*, *Gad1*, and *Sst* among hippocampal neurons (Fig. 3C).

To further test the versatility of TRISCO, we sought to examine the expression patterns of multiple genes frequently used to detect and classify cell types and corresponding tissue-organization principles in the adult mouse brain. We custom designed gene probes targeted to transcripts expressed in distinct cell types, including *Mfge8* mRNA and *Aldoc* mRNA for astrocytes, *Csf1r* mRNA and *Hexb* mRNA for microglia, and *Sox10* mRNA and *Pdgfra* mRNA for oligodendrocytes and their precursors. Typical transcript expression in the aforementioned cell types were readily detectable using TRISCO

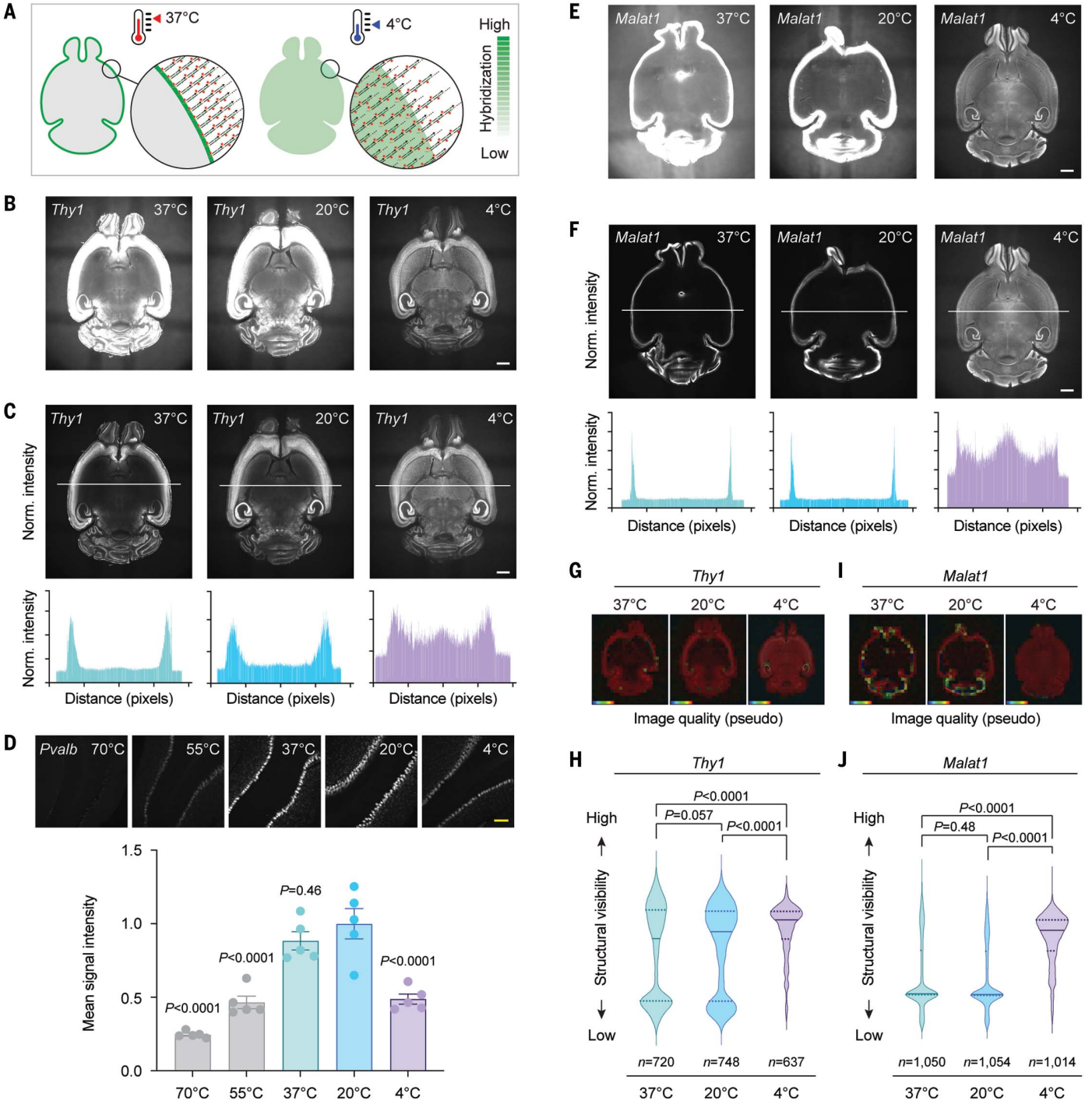

Fig. 2. Improving tissue penetration. (**A**) Schematic showing the isHCR process in a whole brain at 37° (left) and 4°C (right). (**B** and **C**) Optical cross sections of whole brains from 8-week-old mice stained by using isHCR for *Thy1* mRNA at 37°, 20°, and 4°C (B) and normalized images and intensity profiles (below) measured at indicated lines (C). (**D**) Tissue sections of cerebellum stained by using isHCR for *Pvalb* mRNA at 70°, 55°, 37°, 20°, and 4°C and the quantitative analysis of the signal intensities (n = 5 brain sections, one-way ANOVA, $F_{4,20}$ = 28.23, P < 0.0001). The signal intensity was normalized to the mean intensity at 20°C. (**E** and **F**) Optical cross sections of whole brains from 8-week-old mice stained by using isHCR for *Malat1* mRNA at 37°, 20°, and 4°C (E) and normalized images and intensity profiles (below) measured at indicated lines (F). (**G** and **I**) Pseudo-colored image quality analysis of brain cross sections depicted in (C) and (F). Red signifies high-quality regions, whereas blue signifies low-quality regions. (**H** and **J**) Violin plots of the structural visibility at 37°, 20°, and 4°C [one-way ANOVA: (H) $F_{2,2102}$ = 63.59, P < 0.0001; (J) $F_{2,3115}$ = 530.9, P < 0.0001). Scale bars, 1 mm (white) and 100 μm (yellow). All data are shown as the mean ± SEM. Statistical analysis was performed by using one-way ANOVA with Dunnett's (D) or Tukey's [(H) and (J)] post hoc comparison.

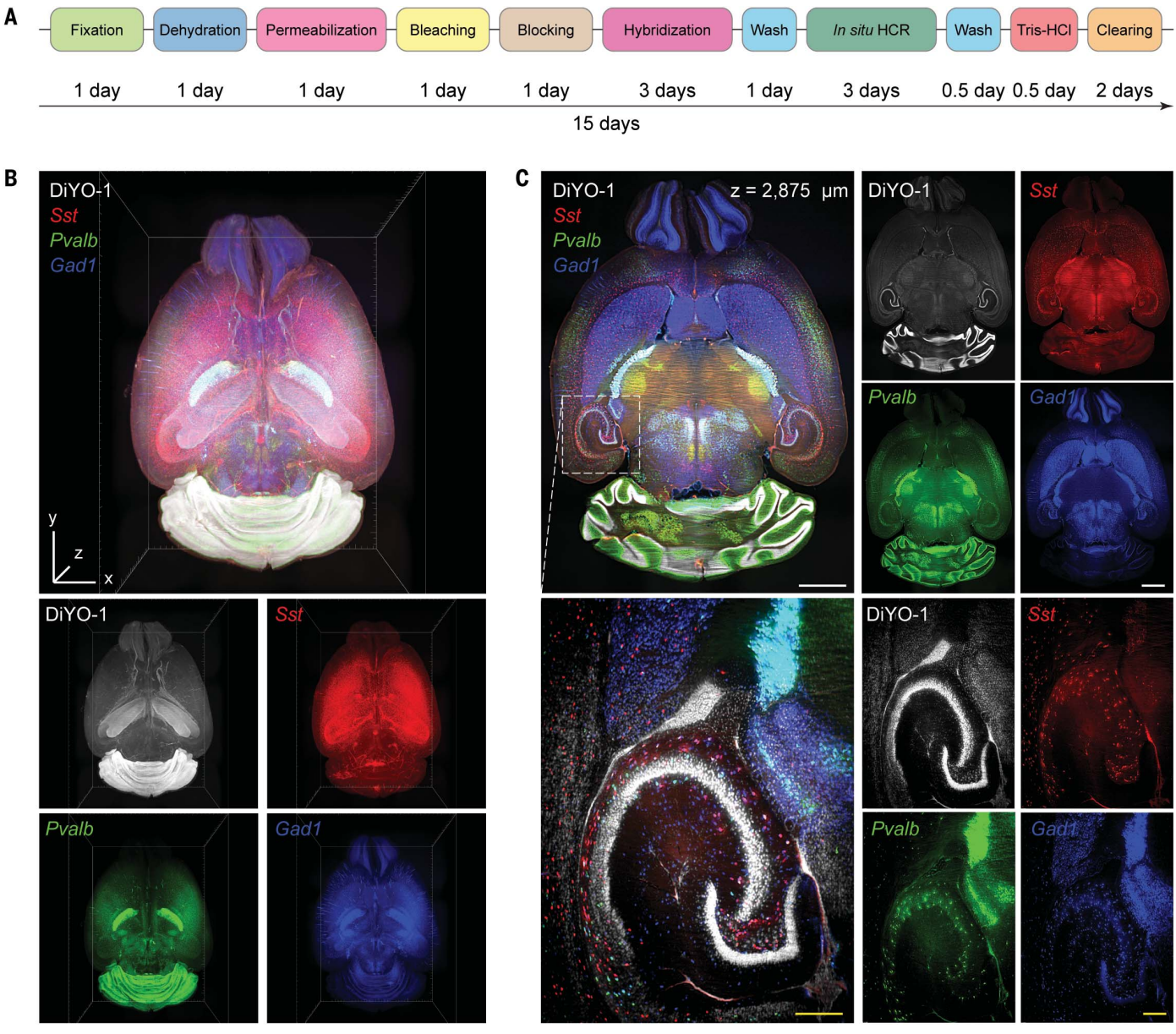

Fig. 3. Multiplexed TRISCO staining of whole brains. (**A**) Schematic of the TRISCO protocol spanning 15 days. (**B**) (Top) 3D rendering of the whole brain from an 8-week-old adult mouse stained using TRISCO for cortical interneuron transcripts: Somatostatin (*Sst* mRNA, red), Parvalbumin (*Pvalb* mRNA, green), and Glutamate decarboxylase 1 (*Gad1* mRNA, blue). (Bottom) Single-channel views. Bounding box, 7.7 × 10.6 × 5.5 mm. (**C**) Optical cross section at z = 2875 µm of the TRISCO brain in (B). (Right) Single-channel views. (Bottom) Magnified views of the hippocampus region at the indicated box. Nuclear staining was done with DiYO-1. Scale bars, 1 mm (white) and 200 µm (yellow).

(Fig. 4A, fig. S4A, and movies S4 to S10). To validate the TRISCO data, we performed experiments on tissue sections stained with conventional isHCR, utilizing the same probes used in the 3D TRISCO experiments (fig. S5). These experiments revealed similar results between TRISCO and conventional isHCR, such as high cell density in the white matter for *Sox10* mRNA and dorsal enrichment of *Mfge8* mRNA (*15*). We also conducted a quantitative analysis using confocal microscopy to count and compare the number of *Csf1r*-positive cells in tissue sections cut from 3D TRISCO-stained brains to those in tissue sections stained using conventional isHCR (fig. S4B). This analysis demonstrated that the percentage of *Csf1r*-positive cells detected in the striatum was nearly identical between the 2D and 3D approaches, suggesting that TRISCO could provide unbiased coverage of the entire region. Additionally, we analyzed the expression of RNA transcripts related to neurotransmitters implicated in higher brain functions, including dopamine, serotonin, and acetylcholine: *Th*, *Slc18a2*, *Slc6a3*, *Tph2*, *Ddc*, *Maoa*, *ChAT*, *Slc13a3*, and *Ache*. TRISCO revealed specific gene expression patterns in deep brain structures, such as the basal ganglia and brainstem (Fig. 4B, fig. S4A, and movies S11 to S20). Volume rendering and magnification further highlighted intricate transcriptional patterns of *Pvalb* mRNA and *Th* mRNA, resolving them at single-cell resolution across the entire mouse brain (movies S21 and S22).

Evaluating TRISCO imaging across mammalian organs and neuronal activity

To expand the potential utility of TRISCO, we performed 3D imaging experiments on various tissues from rodents and humans. Given

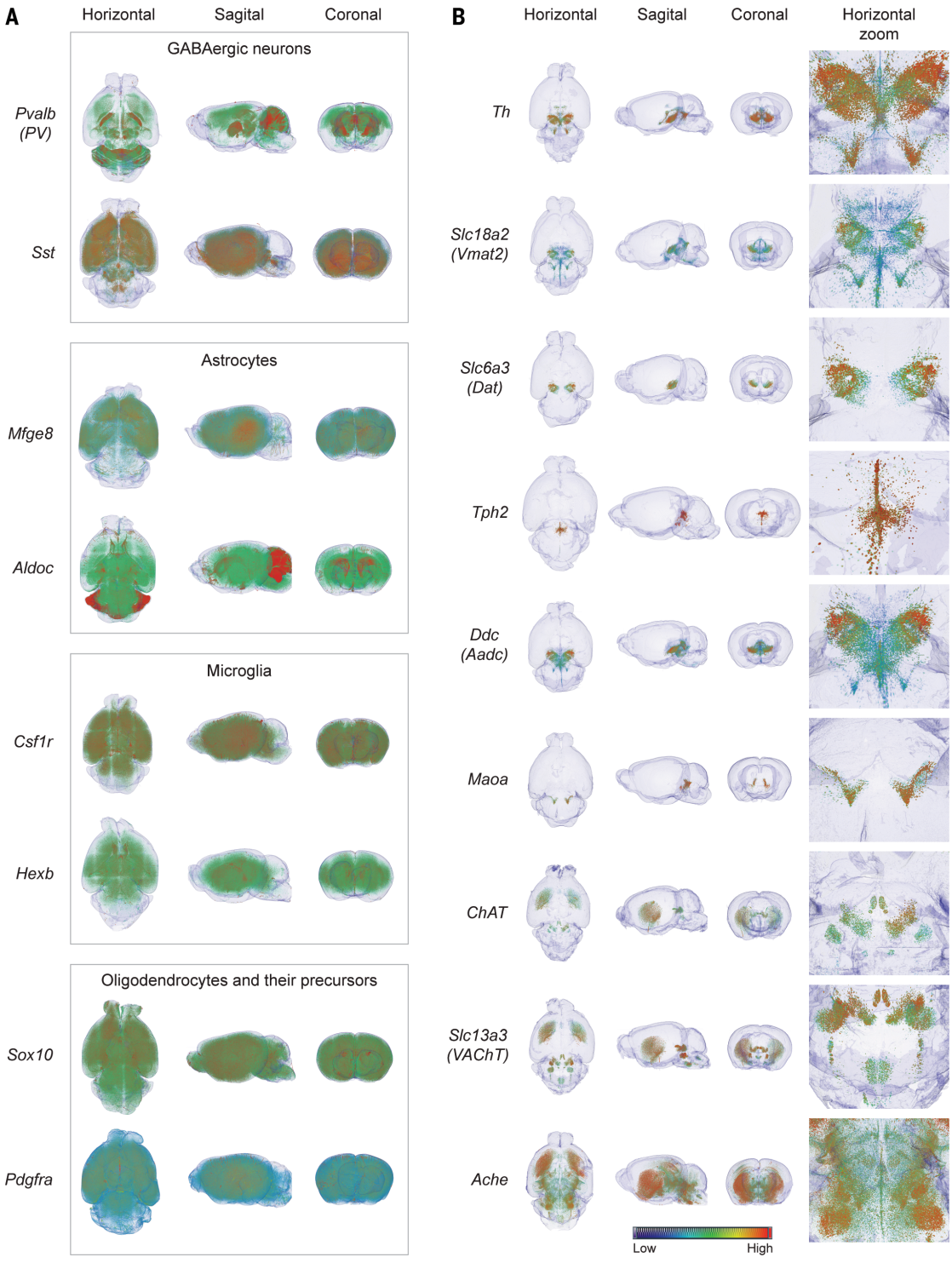

Fig. 4. Whole-brain TRISCO staining of various RNA transcripts. (**A** and **B**) 3D rendered horizontal, sagittal, and coronal views of whole brains from 8-week-old mice stained by using TRISCO for mRNA transcripts detected in GABAergic neurons [*Pvalb* (*PV*) and *Sst*], astrocytes (*Mfge8* and *Aldoc*), microglia (*Csf1r* and *Hexb*), oligodendrocytes and their precursors (*Sox10* and *Pdgfra*) (A), and neurotransmitters *Th*, *Slc18a2* (*Vmat2*), *Slc6a3* (*Dat*), *Tph2*, *Ddc* (*Aadc*), *Maoa*, *ChAT*, *Slc13a3* (*VAChT*), and *Ache* (B). The horizontal and zoomed-in views are from the ventral side. Bounding boxes for all brains are available in fig. S4.

that sample size is the most limiting factor when performing 3D imaging, we explored TRISCO's capacity to perform intact-tissue transcriptional analysis on larger brains, such as those from rats and guinea pigs (Fig. 5A). TRISCO readily visualized *Th* mRNA in the rat brain and *Sst* mRNA in the guinea pig brain without showing signal gradient (Fig. 5B and movies S23 to S25). Optical cross sections of these brains revealed the characteristic expression pattern of *Th* mRNA (Fig. 5C) and *Sst* mRNA (Fig. 5D) at single-cell resolution. We also stained a human fetal brain hemisphere (week 12.5 postconception) for *TBR2* mRNA. TRISCO successfully detected well-defined spatial structures deep inside the human fetal brain, demonstrated by the distinct layering in the subventricular zone (fig. S6). We further tested the versatility of TRISCO by staining organs beyond the brain (fig. S7). In an intact thoracic segment of the mouse spinal cord, we stained for *ChAT* mRNA and effectively detected motor neurons and preganglionic autonomic neurons in the ventral horn. We also performed staining of intact organs outside the central nervous system, such as the heart, kidney, and lung. TRISCO reliably detected

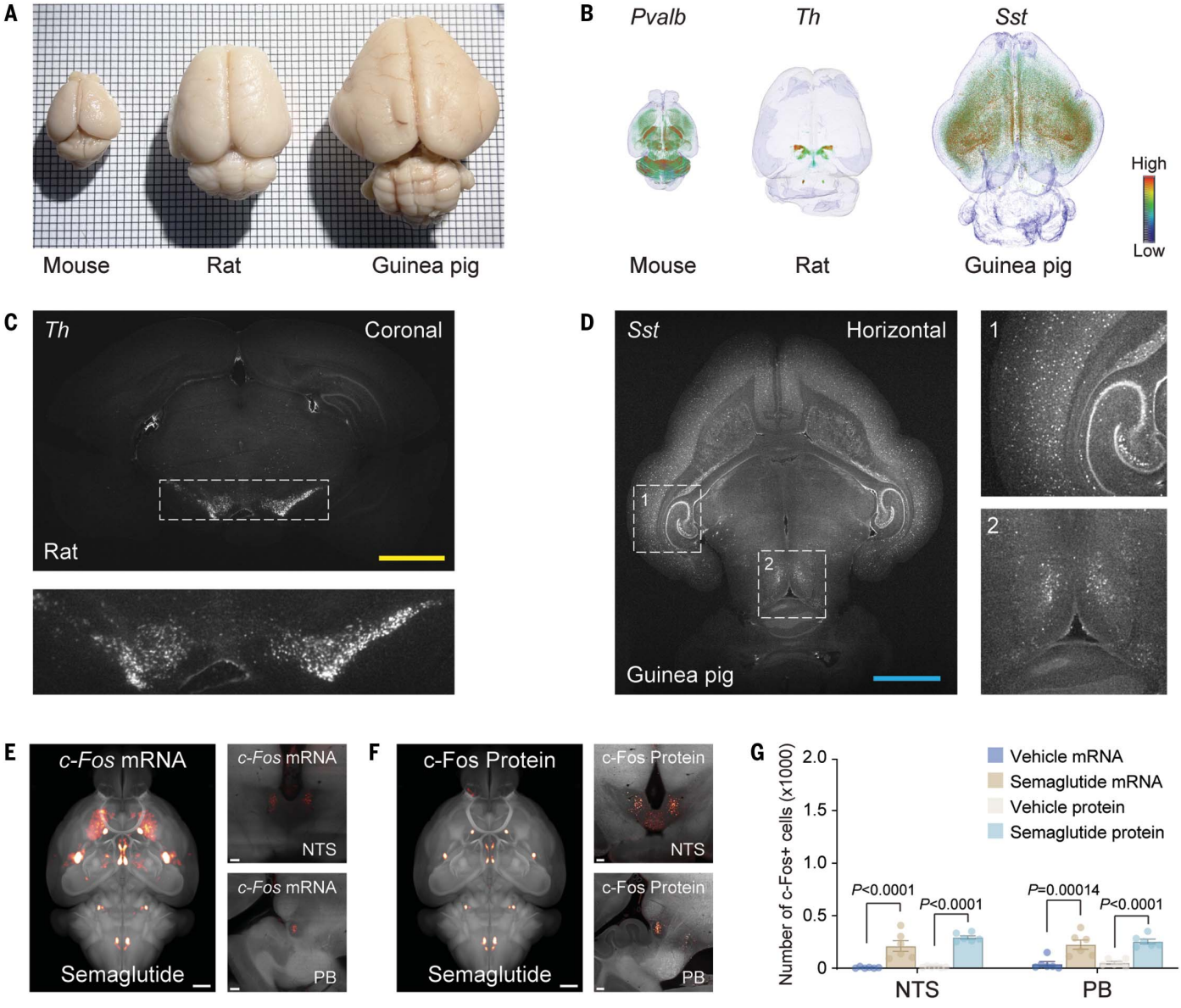

Fig. 5. Whole-brain TRISCO analysis of large rodent brains and neuronal activity by using c-Fos signatures. (**A**) Dissected brains from a mouse, rat, and guinea pig. Grid lines represent 1 mm. (**B**) 3D rendering of TRISCO brains from an 8-week-old mouse stained for *Pvalb* mRNA, a 49-day-old rat stained for *Th* mRNA, and a 2-month-old guinea pig stained for *Sst* mRNA. (**C**) (Top) Optical coronal cross section of the rat brain stained using TRISCO for *Th* mRNA in (B). (Bottom) Magnified view of the indicated box. (**D**) (Left) Optical horizontal cross section of the guinea pig brain stained by using TRISCO for *Sst* mRNA in (B). (Right) Magnified views of indicated boxes. (**E** and **F**) Whole-brain heatmaps of *c-Fos* mRNA expression analyzed with TRISCO (E) and protein expression analyzed with iDISCO (F) upon Semaglutide administration. Zoomed-in views show expression in the nucleus of the solitary tract (NTS) and the parabrachial nucleus (PB). (**G**) Counts of *c-Fos* mRNA and c-Fos protein–positive cells in the NTS and PB of Semaglutide- and vehicle-treated mice. Scalebars, 200 μm (white), 3 mm (yellow), and 5 mm (cyan). All data are shown as the mean ± SEM of n = 6 brains. Statistical analysis was performed by using one-way ANOVA with Dunnett's post hoc comparison test.

tissue-specific RNA transcripts with organ-typical spatial distribution. These results demonstrate that TRISCO is a highly robust tool for analyzing large tissue volumes.

To evaluate the ability of TRISCO to detect functional neuronal activity across the brain, we assessed the expression of the immediate early gene *c-Fos* as a proxy in mice subjected to pharmacological treatments (*14*). First, we confirmed that our probe could detect *c-Fos* mRNA in brain tissue sections from mice that had undergone forced swimming tests (fig. S8, A to C). Then we sought to test whether TRISCO could detect *c-Fos* mRNA in the intact brains of 9-week-old mice following the administration of an acute dose of Semaglutide (*16*), a clinically approved drug used to treat type 2 diabetes and obesity (*17*, *18*). Following this treatment, we observed enhanced *c-Fos* mRNA expression in distinct regions associated with appetite and body weight regulation (Fig. 5E and fig. S8D) compared with that in vehicle-treated animals (fig. S8E). To validate the TRISCO results, we compared the *c-Fos* mRNA expression with c-Fos protein immunostaining using immunolabeling-enabled 3D imaging of solvent-cleared organs (iDISCO) (*14*) (Fig. 5F). For quantitative analysis, we counted and compared *c-Fos* mRNA–positive cells with c-Fos protein–positive cells. This analysis revealed

similar counts of mRNA and protein in the nucleus of the solitary tract and parabrachial nucleus (Fig. 5G).

Collectively, these data demonstrate that TRISCO is a powerful tool for comprehensive investigation of cellular identity, noncoding RNA expression, and activity-regulated gene transcription in whole brains and potentially in other organs as well.

Discussion

The rapid development of various methods and technologies for sequencing and analyzing RNAs in dissociated cells and thin tissue sections has revolutionized biomedical research in general and neuroscience in particular. However, RNA imaging in 3D volumes has traditionally been restricted to smaller sample sizes. Our TRISCO pipeline introduces a powerful new tool in neuroscience that enables 3D spatial analysis of RNA expressions in whole brains, which is currently extremely challenging at best. Whole-brain imaging at cellular resolution offers a wide range of scientific applications, including phenotyping transgenic animals, exploring complex 3D structures such as neuronal circuits and cell niches, assessing activity-regulated gene transcription, and conducting pharmaceutical testing.

3D imaging of large tissue volumes based on immunohistochemistry has been previously reported (*10*, *11*, *19*, *20*). However, visualizing proteins deep within tissue volumes typically presents several challenges, including the limited availability of robust antibodies and the occurrence of signal gradient artifacts from the surface to the core of tissue layers (*14*, *21*). The uniform staining achieved by low-temperature incubation in TRISCO can minimize or even eliminate the need for normalization in image processing, especially for expansive datasets such as entire brains. Furthermore, an added merit of TRISCO is the ability to design and use custom-made probes. As shown in this study, we validated many custom DNA probes (table S1) and confirmed their expression patterns. These include noncoding and protein-coding RNA species whose expression patterns have been challenging or even impossible to study owing to the limited availability of antibodies. Although straightforward, the probe design is versatile enough to encompass a myriad of RNAs. Its simplicity and versatility make TRISCO highly accessible, allowing it to be easily adapted in various laboratory settings without the need for specialized equipment.

As a proof of concept, we demonstrated that TRISCO is not only effective in mouse brains but is also scalable to larger brains, such as those of rats and guinea pigs. This highlights its versatility and applicability beyond smaller animal models. This scalability broadens its potential applications, such as enabling the measurement of brain-wide transcriptional dynamics in larger mammalian species. Furthermore, TRISCO serves as a robust tool for detecting intermediate early genes, enabling the identification of active neurons in specific brain regions, an analysis that is critical for various research fields (*22*, *23*), including pharmaceutical development (*24*). Beyond brain imaging, TRISCO demonstrates broad applicability across various tissues, including the spinal cord, heart, kidney, and lung. This versatility establishes TRISCO as a valuable platform for investigating a wide range of medically relevant questions.

Currently, there are limitations of TRISCO that can be further improved. For example, the signal-to-noise ratio can be enhanced to detect weakly expressed genes. The current version of TRISCO promotes penetration by lowering the temperature, which, to some extent, reduces the amplification kinetics of HCR. TRISCO is still in the improvement stage, and these limitations can be overcome through a deeper understanding of key parameters, such as salt concentration, temperature, probe quantity and diffusion rate, and their effects on tissue penetration and signal amplification. Comprehensive modulation and simulation of these parameters could provide valuable insights, as has been done in previous work (*21*). Additionally, the accessibility of the DNA probe to the target site may be hindered by interference from nearby molecules such as proteins. New sample preparation methods or alternative probe designs will be needed to circumvent this issue.

As multiround isHCR has previously been demonstrated (*25*), we anticipate that optimizing tissue clearing and probe removal in the TRISCO protocol will enable multiround analysis and, therefore, greater multiplexing capabilities. However, with the timeline of the current technology, it is impractical to achieve high-content multiplexing in this manner. Nonetheless, there is strong potential for improvement. By accelerating protocols, such as developing faster HCR reaction methods and enhancing probe penetration, this technique could become highly practical for widespread use. Additionally, creating new methods that can reliably detect RNAs even after repeated harsh treatments would facilitate multiround experiments. Addressing these challenges and automating the entire protocol could lead to the development of a high-content 3D imaging method comparable to current spatial transcriptomics analysis on 2D tissue sections.

Taken together, the development of TRISCO marks a substantial advancement in high-performance imaging, unlocking access to a vast and untapped reservoir of 3D transcriptional data. The depth and breadth of information that TRISCO provides enables a more detailed and holistic view of gene expression within intact brains. By enabling the volumetric visualization and analysis of RNA transcripts, TRISCO bridges a critical gap in neuroscience research, linking the neural transcript profiles with spatial coordinates to explore the dynamic and complex landscape of the brain.

REFERENCES AND NOTES

1. P. Ariel, *Int. J. Biochem. Cell Biol.* **84**, 35–39 (2017).
2. H. R. Ueda *et al*., *Nat. Rev. Neurosci.* **21**, 61–79 (2020).
3. E. L. Sylwestrak, P. Rajasethupathy, M. A. Wright, A. Jaffe, K. Deisseroth, *Cell* **164**, 792–804 (2016).
4. T. Tian, Z. Yang, X. Li, *J. Anat.* **238**, 489–507 (2021).
5. N. Tanaka *et al*., *Nat. Biomed. Eng.* **4**, 875–888 (2020).
6. J. Temsamani, S. Agrawal, *Mol. Biotechnol.* **5**, 223–232 (1996).
7. R. M. Dirks, N. A. Pierce, *Proc. Natl. Acad. Sci. U.S.A.* **101**, 15275–15278 (2004).
8. H. M. Choi, V. A. Beck, N. A. Pierce, *ACS Nano* **8**, 4284–4294 (2014).
9. H. M. T. Choi *et al*., *Development* **145**, dev165753 (2018).
10. A. Ertürk *et al*., *Nat. Protoc.* **7**, 1983–1995 (2012).
11. N. Renier *et al*., *Cell* **159**, 896–910 (2014).
12. P. Chomczynski, *Nucleic Acids Res.* **20**, 3791–3792 (1992).
13. C. C. Earl, M. T. Smith, R. A. Lease, B. C. Bundy, *Bioengineered* **9**, 90–97 (2018).
14. N. Renier *et al*., *Cell* **165**, 1789–1802 (2016).
15. A. Zeisel *et al*., *Cell* **174**, 999–1014.e22 (2018).
16. S. Gabery *et al*., *JCI Insight* **5**, e133429 (2020).
17. M. Davies *et al*., *Lancet* **397**, 971–984 (2021).
18. J. P. H. Wilding *et al*., *N. Engl. J. Med.* **384**, 989–1002 (2021).
19. N. Tanaka *et al*., *Nat. Biomed. Eng.* **1**, 796–806 (2017).
20. E. A. Susaki *et al*., *Cell* **157**, 726–739 (2014).
21. C. N. Yau *et al*., *Cell Rep. Methods* **3**, 100458 (2023).
22. J. I. Morgan, T. Curran, *Trends Neurosci.* **12**, 459–462 (1989).
23. M. Sheng, M. E. Greenberg, *Neuron* **4**, 477–485 (1990).
24. J. Perens, J. Hecksher-Sørensen, *Front. Neurosci.* **16**, 866884 (2022).
25. C. M. Tatsuya, H. Nathaniel, Multiplexed and scalable cellular phenotyping toward the standardized three-dimensional human neuroanatomy. bioRxiv 2022.2011.2023.517711 [Preprint] (2022); https://doi.org/10.1101/2022.11.23.517711.

ACKNOWLEDGMENTS

We thank M. Bertho, P. Löw, O. Kiehn, J. Bruton, and K. Jardemark from Karolinska Institutet, Stockholm, Sweden, for providing us with mouse and rat brains, and we acknowledge Uhlén lab members for critical feedback. We would like to acknowledge the service by the Karolinska Institutet Developmental Tissue Bank in providing the human fetal brain tissue used in this study. The light-sheet microscopy infrastructure used in this research received grants from the Strategic Research Area in Neuroscience (StratNeuro) and the Strategic Research Area in Stem Cells and Regenerative Medicine (StratRegen), supported by the Swedish government. **Funding:** Swedish Research Council 2017-00815 (P.U.); Swedish Research Council 2021-03108 (P.U.); Swedish Brain Foundation FO2018-0209 (P.U.); Swedish Brain Foundation FO2020-0199 (P.U.); Swedish Cancer Society 19 0544 Pj (P.U.); Swedish Cancer Society 19 0545 Us (P.U.); Swedish Cancer Society 22 2454 Pj (P.U.); Swedish Childhood Cancer Foundation PR2020-0124 (P.U.); Swedish Childhood Cancer Foundation PR2022-0111 (P.U.); Cancer Research Foundations of Radiumhemmet 201362 (P.U.); Cancer Research Foundations of Radiumhemmet 221353 (P.U.); Wenner-Gren foundation UPD2022-0159 (P.U.); Swedish Research Council grant 2023-00324 (G.C.B.); Knut and Alice Wallenberg Foundation grant 2023-0280 (G.C.B.); European Committee for Treatment and Research in Multiple Sclerosis (ECTRIMS) (L.R.R.-K.); National MS Society (NMSS, USA, TA-2305-41342) (L.R.R.-K.); **Author contributions:** S.K., J.C.K., Y.L., Z.W., D.V.N., D.K., K.F., R.K., I.E., K.T., L.R.R.-K., and S.Z. performed experiments and analyzed data. L.L.L., J.L.S., C.G.S., and U.R. performed Semaglutide experiments and analyzed data. U.R. and J.H.S. supervised the Semaglutide experiments. X.L., E.S., and J.H. provided human tissue. L.R.R.-K., G.C.-B., Y.X., and M.A. provided rodent tissue. A.W., D.H.T., N.U., T.T., and A.M. provided conceptual advice. S.K. designed experiments. P.U. acquired funding and supervised the study. S.K. and P.U. conceived the

project and wrote the manuscript with input from all authors. **Competing interests:** L.L.L., J.L.S., C.G.S., J.H.S., and U.R.O. are employees and hold shares at Gubra. The other authors declare that they have no completing interests. **Data and materials availability:** All data are available in the main text or the supplementary materials. **License information:** Copyright © 2024 the authors, some rights reserved; exclusive licensee American Association for the Advancement of Science. No claim to original US government works. https://www.science.org/about/science-licenses-journal-article-reuse

SUPPLEMENTARY MATERIALS

science.org/doi/10.1126/science.adn9947
Materials and Methods
Figs. S1 to S8
Table S1
References (*26*–*30*)
MDAR Reproducibility Checklist
Movies S1 to S26

Submitted 16 January 2024; accepted 18 October 2024
10.1126/science.adn9947